Molecular Microbiology (2019) 112(5), 1423–1439

doi:10.1111/mmi.14369
First published online 24 September 2019

A gradient-forming MipZ protein mediating the control of cell division in the magnetotactic bacterium *Magnetospirillum gryphiswaldense*

Mauricio Toro-Nahuelpan,[1,2,†,‡] Laura Corrales-Guerrero,[3,‡] Theresa Zwiener,[1] Manuel Osorio-Valeriano,[3,4] Frank-Dietrich Müller,[1] Jürgen M. Plitzko,[2] Marc Bramkamp,[5] Martin Thanbichler[3,4,6*] and Dirk Schüler[1*]

[1] *Institute of Microbiology, University of Bayreuth, Bayreuth, Germany.*
[2] *Department of Molecular Structural Biology, Max Planck Institute of Biochemistry, Planegg-Martinsried, Germany.*
[3] *Faculty of Biology, Philipps-Universität, Marburg, Germany.*
[4] *Max Planck Fellow Group "Bacterial Cell Biology", Max Planck Institute for Terrestrial Microbiology, Marburg, Germany.*
[5] *Department of Biology I, Ludwig-Maximilians-Universität München, Planegg-Martinsried, Germany.*
[6] *Center for Synthetic Microbiology, Marburg, Germany.*

Summary

Cell division needs to be tightly regulated and closely coordinated with other cellular processes to ensure the generation of fully viable offspring. Here, we investigate division site placement by the cell division regulator MipZ in the alphaproteobacterium *Magnetospirillum gryphiswaldense*, a species that forms linear chains of magnetosomes to navigate within the geomagnetic field. We show that *M. gryphiswaldense* contains two MipZ homologs, termed MipZ1 and MipZ2. MipZ2 localizes to the division site, but its absence does not cause any obvious phenotype. MipZ1, by contrast, forms a dynamic bipolar gradient, and its deletion or overproduction cause cell filamentation, suggesting an important role in cell division. The monomeric form of MipZ1 interacts with the chromosome partitioning protein ParB, whereas its ATP-dependent dimeric form shows non-specific DNA-binding activity. Notably, both the dimeric and, to a lesser extent, the monomeric form inhibit FtsZ polymerization *in vitro*. MipZ1 thus represents a canonical gradient-forming MipZ homolog that critically contributes to the spatiotemporal control of FtsZ ring formation. Collectively, our findings add to the view that the regulatory role of MipZ proteins in cell division is conserved among many alphaproteobacteria. However, their number and biochemical properties may have adapted to the specific needs of the host organism.

*For correspondence. E-mails dirk.schueler@uni-bayreuth.de (D. Schüler); Tel. +49 921 552729; Fax +49 921 552727; thanbichler@uni-marburg.de (M. Thanbichler); Tel. +49 6421 2821809; Fax +49 6421 2821832. [†]Present address: European Molecular Biology Laboratory, Heidelberg, Germany. [‡]Mauricio Toro-Nahuelpan and Laura Corrales-Guerrero contributed equally to this work.

Introduction

Magnetotactic bacteria are a diverse group of organisms that have the ability to align along the geomagnetic field lines. This property is mediated by chains of membrane-bounded magnetic crystals, known as magnetosomes, which act as nanoscale compass needles (Uebe and Schüler, 2016). In the alphaproteobacterium *Magnetospirillum gryphiswaldense* as well as related magnetospirilla, magnetosomes are concatenated into a highly ordered linear array (Uebe and Schüler, 2016). Their formation is mediated by dedicated cytoskeletal elements, termed the 'magnetoskeleton', which comprises the actin-like MamK filament, the adapter protein MamJ and the localization factor MamY (Komeili *et al.*, 2006; Scheffel *et al.*, 2006; Toro-Nahuelpan *et al.*, 2016; 2019). Throughout the cell cycle of *M. gryphiswaldense*, the magnetosome chain is oriented parallel to the long axis of the spirilloid cell, with the chain center positioned dynamically at midcell (Katzmann *et al.*, 2011; Toro-Nahuelpan *et al.*, 2016; Uebe and Schüler, 2016). During cell division, the magnetosome chain becomes equipartitioned to efficiently pass on the selective advantage of magnetotaxis to both daughter cells (Katzmann *et al.*, 2011). Once cytokinesis is finished, the partitioned chains are repositioned from the new cell poles to the cell center by the pole-to-midcell-directed treadmilling of MamK filaments

(Katzmann *et al*., 2011; Toro-Nahuelpan *et al*., 2016). The formation and splitting of magnetosome chains need to be closely coordinated with cell division in time and space. However, so far, the mechanisms that control the division process in *M. gryphiswaldense* remain poorly understood.

In most bacteria, the site of cell division is marked by a discontinuous ring-like polymeric assembly of the tubulin homolog FtsZ (Bi and Lutkenhaus, 1991; Ben-Yehuda and Losick, 2002; Li *et al*., 2007). This so-called Z-ring recruits, directly and indirectly, all other components of the cell division apparatus and plays a central regulatory role in the constriction process (Erickson *et al*., 2010; Bisson-Filho *et al*., 2017; Yang *et al*., 2017). Unlike most other bacteria, *M. gryphiswaldense* possesses two FtsZ homologs: a canonical FtsZ and a C-terminally truncated variant termed FtsZm. Previous studies have shown that the canonical FtsZ homolog plays an essential role in cell division (Ding *et al*., 2010; Müller *et al*., 2014). Furthermore, cryo-electron tomography (cryo-ET) analysis of the cell division site of *M. gryphiswaldense* revealed arc-like structures that may represent a discontinuous Z-ring driving the typical asymmetric constriction observed for this species (Katzmann *et al*., 2011; Yao *et al*., 2017). Similar to the canonical FtsZ protein, its paralog FtsZm shows GTPase activity, and it is able to form homo- and heteropolymers with FtsZ *in vitro*. However, FtsZm does not appear to be involved in cell division but rather has a role in magnetosome biomineralization, consistent with the fact that its gene is located within a magnetosome-related operon (Ding *et al*., 2010; Müller *et al*., 2014).

To ensure proper cell division, Z-ring formation needs to be tightly regulated in time and space. In many bacteria, this task is achieved by the prototypical Min and nucleoid occlusion systems, which prevent the polymerization of FtsZ at the cell poles or over the nucleoid respectively (Marston *et al*., 1998; Raskin and de Boer, 1999; Wu and Errington, 2004; 2011; Bernhardt and de Boer, 2005; Lutkenhaus, 2007). However, these systems are poorly conserved among the *Alphaproteobacteria*. Min proteins, for instance, are only found in some members of the orders *Rhizobiales*, *Rhodobacterales* and *Rhodospirillales* (Flores *et al*., 2018), suggesting the existence of other mechanisms to control cell division in the alphaproteobacterial lineage.

An alternative cell division regulator identified in the *Alphaproteobacteria* is the protein MipZ from *Caulobacter crescentus*. MipZ is a P-loop ATPase that forms a bipolar gradient, with concentration maxima at the cell poles and a minimum at the cell center (Thanbichler and Shapiro, 2006). It acts as an inhibitor of FtsZ polymerization and thus prevents Z-ring assembly in the polar regions of the cell, thereby limiting cell division to the cell center. Loss of MipZ triggers the formation of multiple mispositioned FtsZ assemblies that initiate acentric cell division events, producing a mixture of elongated and mini cells (Thanbichler and Shapiro, 2006). The function of MipZ relies on its interaction with the nucleoid and the DNA partitioning protein ParB, which recognizes a cluster of specific binding sites (*parS*) in the chromosomal origin region (Thanbichler and Shapiro, 2006; Kiekebusch *et al*., 2012). After entry of the cells into S-phase, the two sister origin regions of *C. crescentus* re-associate with ParB and then become immobilized at opposite cell poles. The polar ParB·*parS* complexes interact with freely diffusible MipZ monomers and induce their ATP-dependent dimerization. The resulting dimers dissociate from ParB and bind non-specifically to the surrounding chromosomal DNA, where they inhibit Z-ring assembly. Spontaneous ATP hydrolysis then triggers their disassembly into monomers, which leave the DNA and finally re-associate with ParB at the cell poles, starting a new localization cycle (Thanbichler and Shapiro, 2006; Kiekebusch *et al*., 2012).

Remarkably, in the alphaproteobacterium *Rhodobacter sphaeroides*, MipZ shows a very different behavior. While its monomeric form dynamically interacts with the cell pole-associated ParB·*parS* complexes, dimers consistently colocalize with FtsZ, forming an annular structure that lines the inner side of the Z-ring throughout the constriction process (Dubarry *et al*., 2019). The recruitment of the protein to midcell depends on the presence of FtsZ, and its overproduction leads to cell filamentation and the formation of mini cells. These findings suggest that *R. sphaeroides* MipZ represents a second class of MipZ proteins that may control the stability or dynamics rather than the subcellular localization of the Z-ring. Although MipZ proteins are conserved in the majority of alphaproteobacteria, it is currently unknown whether they belong to any of the two previously identified classes or have adopted different roles in cell division.

In this study, we identify two MipZ homologs in *M. gryphiswaldense*. We show that loss or overproduction of MipZ1 lead to a severe impairment of cell division. Live cell imaging and photokinetic analyses reveal that the MipZ1 uses ATP binding and hydrolysis to establish a highly dynamic, bipolar gradient. Gradient formation depends on the interaction of MipZ1 with ParB and its non-specific association with chromosomal DNA. Importantly, MipZ1 stimulates the GTPase activity of FtsZ and abolishes FtsZ polymerization *in vitro*. It therefore appears to act as a critical negative regulator of cell division that coordinates cell division with chromosome segregation in *M. gryphiswaldense*. MipZ2, by contrast, colocalizes with FtsZ throughout the course of the cell cycle, but its inactivation does not cause any obvious phenotype, suggesting an accessory role in the division process. Collectively, our results demonstrate that *M. gryphiswaldense* employs two functional MipZ homologs. Moreover, they support the idea that the regulatory role of MipZ proteins in

cell division is conserved among alphaproteobacteria, although their mechanism of action and importance may vary between species.

Results

MipZ1, but not MipZ2, is critical for proper cell division in M. gryphiswaldense

Searching the genomic sequence of *M. gryphiswaldense* for potential cell division regulators, we were unable to detect a Min system or homologs of known nucleoid occlusion proteins. However, we identified two *mipZ*-like genes (locus tags MGR_4222 and MGR_0570), which encode genuine members of the MipZ subfamily of the Mrp/MinD ATPases (Fig. S1A). MipZ1 (MGR_4222) and MipZ2 (MGR_0570) exhibit 46% and 43% sequence identity (65% and 64% similarity), respectively, to MipZ from *C. crescentus* ($MipZ_{Cc}$) (Fig. S1B). Moreover, the two proteins share 45% identity (63% similarity) with each other. Modeling studies with the crystal structure of $MipZ_{Cc}$ (Kiekebusch *et al.*, 2012) as a template suggested a high structural similarity of the MipZ homologs from *M. gryphiswaldense* to $MipZ_{Cc}$, with root-mean-square deviation (rmsd) values of 0.62 Å (239 atoms) for MipZ1 and 0.62 Å (225 atoms) for MipZ2 (Figure S1C). The predicted structures of MipZ1 and MipZ2 were almost superimposable, with an rmsd of 0.43 Å (224 atoms). To address the role of the two MipZ homologs, we first generated an *M. gryphiswaldense* strain bearing an in-frame deletion

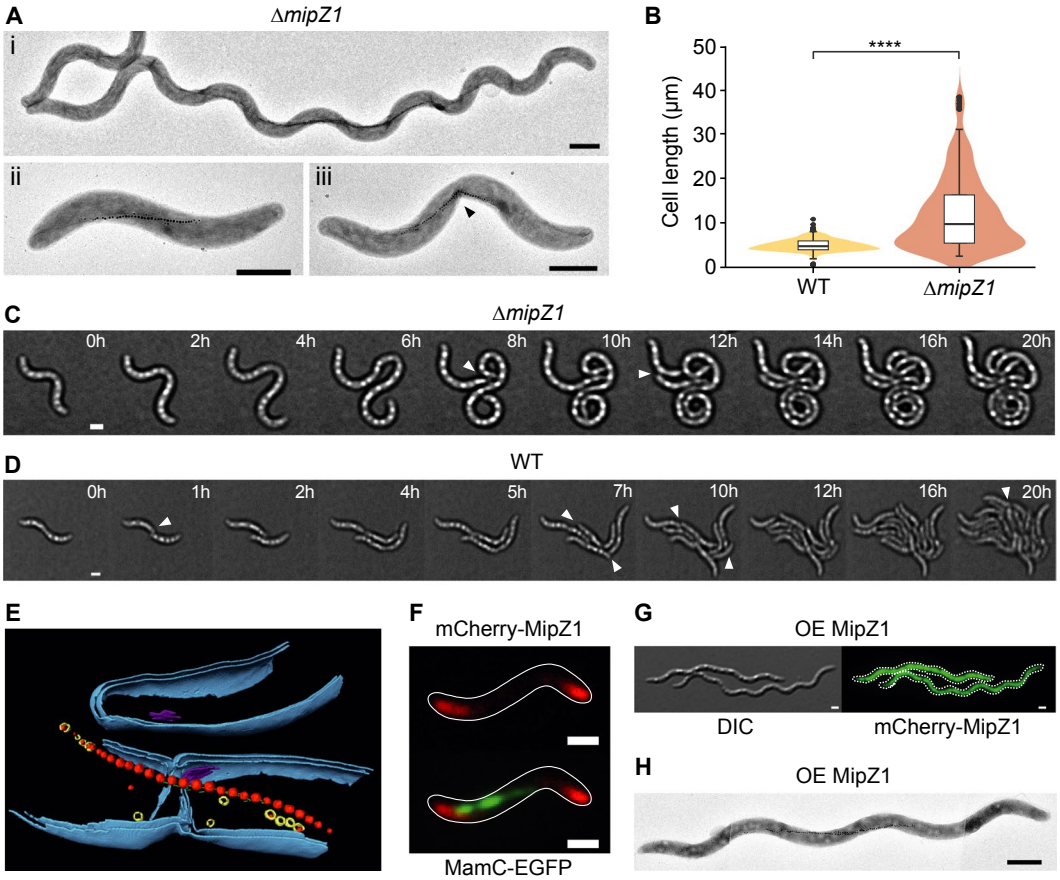

Fig. 1. The absence or mislocalization of MipZ1 impairs cell division.
A. Transmission electron micrographs of the Δ*mipZ1* mutant (TZ001) showing elongated cells with medial (i-ii) and equally partitioned (iii-black arrowhead) magnetosome chains.
B. Cell length distribution of the WT and Δ*mipZ1* strains. The data are represented as box plots, with the thick horizontal line indicating the median, the box the interquartile range and the whiskers extending to the lowest and highest value within 1.5 times the interquartile range from the hinges respectively. In addition, rotated kernel density plots (orange) are given for each dataset to indicate the distribution of the data (****$p < 0.0001$; Student's *t*-test). $n = 522$ cells (WT) and 340 cells (Δ*mipZ1*).
C and D. Time-lapse microscopic analysis of the Δ*mipZ1* (C) and WT (D) strains (white arrowheads indicate divided cells).
E. 3D surface rendering of cryo-electron tomograms depicting the cell division site in a Δ*mipZ1* cell. Magnetite crystals: red; magnetosome membrane vesicles: yellow; actin-like MamK filament: green; chemoreceptor arrays: purple; inner and outer membrane: blue.
F. Subcellular localization of mCherry-MipZ1 and the magnetosome chain (MamC-EGFP) by fluorescence microscopy in strain eMTN023.
G. DIC and fluorescence images of a strain (eMTN025) overexpressing the *mipZ1* gene. mCherry fluorescence is depicted in green.
H. Transmission electron micrograph of an elongated cell overproducing MipZ1 (composed of three stitched micrographs). Scale bars: 1 μm.

of the *mipZ1* gene. Reminiscent of the Δ*mipZ* phenotype observed for *C. crescentus* (Thanbichler and Shapiro, 2006; Radhakrishnan *et al*., 2010) and *Brevundimonas subvibrioides* (Curtis and Brun, 2014), the mutation lead to the formation of highly elongated cells (Fig. 1Ai-iii and B), indicating that MipZ1 is required for the correct timing and/or spatial regulation of cell division. In both filamentous and normal-sized Δ*mipZ1* cells, magnetosome chains appeared to be properly positioned at midcell (Fig. 1Ai-ii) and evenly partitioned to the daughter cells (Fig. 1Aiii). Time-lapse analysis confirmed that the mutant formed elongated cells that divided only sporadically and in a highly asymmetric fashion, producing filamentous cells of variable length (Fig. 1C). In the wild type, by contrast, cell division consistently occurred around midcell and thus resulted in daughter cells of approximately equal size (Fig. 1D), in agreement with previous results (Katzmann *et al*., 2011). Notably, the cell division defect of the Δ*mipZ1* mutant was accompanied by a significant increase in its doubling time (5.4 ± 0.3 h as compared to 4.1 ± 0.1 h for the wild-type strain; average of three growth curves; ± SD). To further characterize the mutant phenotype, we imaged the constriction site of dividing Δ*mipZ1* filaments by cryo-electron tomography. 3D rendering of specific subcellular structures revealed the characteristic unidirectional invagination of the cell envelope described previously for *M. gryphiswaldense* (Katzmann *et al*., 2011; Toro-Nahuelpan *et al*., 2016), with the magnetosome chain centered at midcell (Figs 1E and S2A–E, Movie S1). Thus, the cell division defect observed is likely due to an abnormal spatiotemporal regulation of divisome assembly rather than a block in the division process itself.

To determine how MipZ1 can affect the regulation of cell division, we tagged the protein with the red fluorescent protein mCherry and determined its subcellular localization by fluorescence microscopy. Interestingly, in pre-divisional cells, the fusion formed a bipolar gradient, with the signal intensities peaking at the cell poles and gradually decreasing toward the cell center (Fig. 1F), reminiscent of the pattern observed for the *C. crescentus* MipZ homolog (Thanbichler and Shapiro, 2006). Upon overproduction of the fusion protein, gradient formation was abolished and mCherry-MipZ1 was evenly distributed throughout the cell (Fig. 1G). Under these conditions, the cells were markedly elongated (Fig. 1H) and failed to form constrictions. However, the recruitment of the magnetosome chain to midcell remained unaffected. These findings suggest that MipZ1 has a negative regulatory effect on cell division.

Next, we set out to characterize the function of the second MipZ homolog of *M. gryphiswaldense*. Unlike the Δ*mipZ1* mutant, a strain carrying an in-frame deletion of the *mipZ2* gene produced normal-sized cells (Fig. 2Ai and B) with a generation time similar to that of the wild-type strain (3.9 ± 0.03 h; average of three growth curves). Moreover, time-lapse imaging and TEM analysis did not reveal any apparent defect in cell division or in the positioning and segregation of magnetosome chains (Fig. 2Ai-ii, B and C). Finally, cryo-ET revealed that Δ*mipZ2* cells still displayed the characteristic asymmetric constriction as they underwent cytokinesis (Fig. S2F-K and Movie S2), indicating that cell division proceeded normally in this background. Similarly, overproduction of MipZ2 did not affect cell length (4.2 ± 0.9 μm for the wild-type strain compared to 4.4 ± 0.9 μm for a *mipZ2*-overexpressing strain; n = 33 cells) or cause any other obvious morphological defects, supporting the notion that this protein has no or only a minor role in the regulation of the division process.

To test whether MipZ1 and MipZ2 have redundant functions, we constructed a strain carrying in-frame deletions in both *mipZ*-like genes. Whole genome sequencing and single nucleotide polymorphism analyses verified the absence of suppressor mutations in coding regions. The double mutant formed elongated cells of variable length, essentially phenocopying the Δ*mipZ1* single mutant (Fig. 2D). Again, the magnetosome chain was properly localized at the cell center and appeared to be partitioned equally to the daughter cells. Time-lapse imaging showed that filamentous cells formed by the double mutant underwent only sporadic asymmetric division events (Fig. 2E), reminiscent of the phenotype observed for Δ*mipZ1* cells. Collectively, these results suggest that only MipZ1 has a critical role in *M. gryphiswaldense* cell division.

To evaluate the subcellular distribution of MipZ2 and correlate its behavior to that of MipZ1, we generated a strain producing both an mCherry-MipZ2 and an eGFP-MipZ1 fusion. We then analyzed the localization patterns of the two proteins in cells at different stages of the cell cycle. In newborn cells, MipZ1 localized to one of the cell poles, whereas MipZ2 was detected at the opposite end of the cell. Intriguingly, MipZ2 also displayed a gradient pattern (Fig. 2F). Later in the cell cycle, the MipZ1 focus duplicated and one of the copies moved in direction of the pole occupied by MipZ2 (compare also Fig. 5A). Concomitant with the arrival of MipZ1, which now formed a bipolar gradient, most of the MipZ2 population was displaced from its original polar position and localized to midcell, where it remained until cytokinesis took place. However, in pre-divisional cells, a small fraction of the protein was also detected at the two cell poles (Fig. 2F). Thus, both MipZ homologs of *M. gryphiswaldense* show cell cycle-dependent localization dynamics, but their distribution patterns are strikingly different.

We next compared the positioning of MipZ2 to that of FtsZ, using eGFP-MipZ2 and FtsZ-mCherry fusions. In new-born (short) cells, MipZ2 co-localized with FtsZ at one of the poles (Fig. 2G). Early in the cell cycle, FtsZ relocated to the cell center where it initially remained poorly focused. This step was followed by the gradual

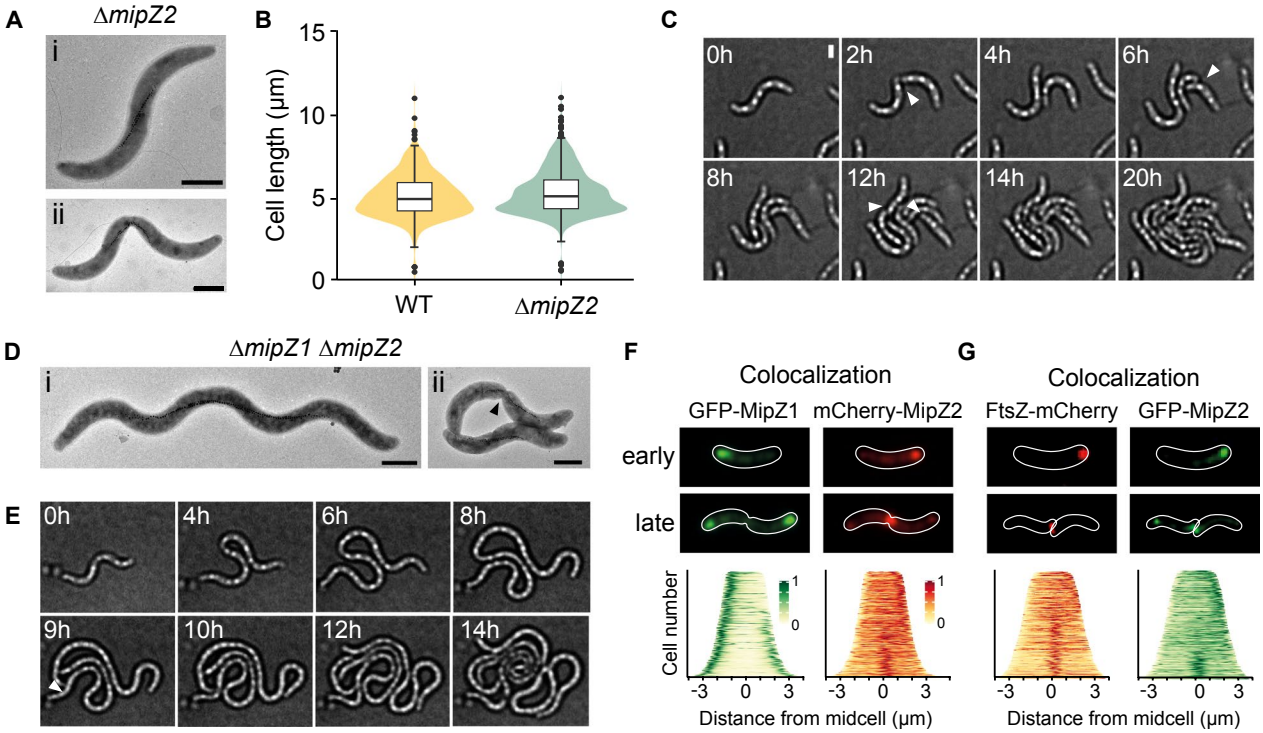

Fig. 2. Phenotypes of the Δ*mipZ2* and Δ*mipZ1* Δ*mipZ2* mutants.
A. Transmission electron micrographs of the Δ*mipZ2* mutant (MT024) showing WT-like cells with medial magnetosome chains (i) that are evenly segregated upon division (ii).
B. Cell length distribution of the WT and Δ*mipZ2* strains. The data are represented as box plots and rotated kernel density plots, as described in Fig. 1B. *n* = 522 cells (WT) and 1021 cells (Δ*mipZ2*).
C. Time-lapse microscopic analysis of the Δ*mipZ2* strain (white arrowheads indicate divided cells).
D. TEM images of the Δ*mipZ1* Δ*mipZ2* double deletion mutant (TZ003) displaying filamentous and WT-like cells with medial magnetosome chains that are evenly segregated upon division (ii, black arrowhead).
E. Time-lapse microscopic analysis of the Δ*mipZ1* Δ*mipZ2* strain (white arrowheads indicate divided cells). Scale bars: 1 μm.
F. Subcellular localization of eGFP-MipZ1 and mCherry-MipZ2 (strain FM98). Shown are representative cells at an early and late stage of the cell cycle. The graphs show a demographic analysis of the cells. To generate it, fluorescence intensity profiles obtained from a representative subpopulation of cells (*n* = 251 cells) were normalized, sorted according to cell length and stacked on top of each other.
G. Subcellular localization of eGFP-MipZ2 and FtsZ-mCherry (strain FM100). Shown are representative cells at an early and late stage of the cell cycle. The graphs show a demographic analysis of the cells, generated as described in (F) (*n* = 286 cells).

redistribution of MipZ2 to the division site. Notably, a stable FtsZ focus was only detected once MipZ2 has accumulated at midcell, which opens the possibility that MipZ2 could have a stabilizing effect on Z-ring formation. A similar sequence of events was observed when the two fusions were produced in the Δ*mipZ1* Δ*mipZ2* background (Fig. S3). However, the Z-ring appeared to form much later in the cell cycle compared to the wild-type strain (Fig. S3), likely due to the absence of regulatory effect of MipZ1. Moreover, FtsZ-mCherry fluorescence was rather faint at all stages of the cell cycle. These results further support the notion that MipZ1 is essential for the proper FtsZ localization in *M. gryphiswaldense*.

MipZ1 forms a dynamic gradient that depends on its ATPase activity

The gradient-like pattern observed for mCherry-MipZ1 is likely to be the result of a dynamic process. To obtain insight into the underlying mechanism, we studied the mobility of the fusion protein in the wild-type background using fluorescence recovery after photobleaching (FRAP) analysis. When one of the polar signals was bleached in cells showing a bipolar MipZ1 gradient, fluorescence was recovered with a half-time ($t_{½}$) of ~ 13 s (Fig. 3A and B), while the intensity of the signal at the opposite pole decreased proportionally. After equilibration, both poles displayed similar signal intensities. The complete equilibration of the fluorescence signal indicates that all MipZ1 molecules were mobile, and rapidly exchanged between the two polar populations. The same dynamics were observed when MipZ1 was produced in a Δ*mipZ1* mutant background, validating the functionality of the mCherry-tagged protein (Fig. S4A).

To test for a functional interaction between the two MipZ homologs from *M. gryphiswaldense*, we examined the dynamics of mCherry-MipZ1 in the Δ*mipZ2* mutant

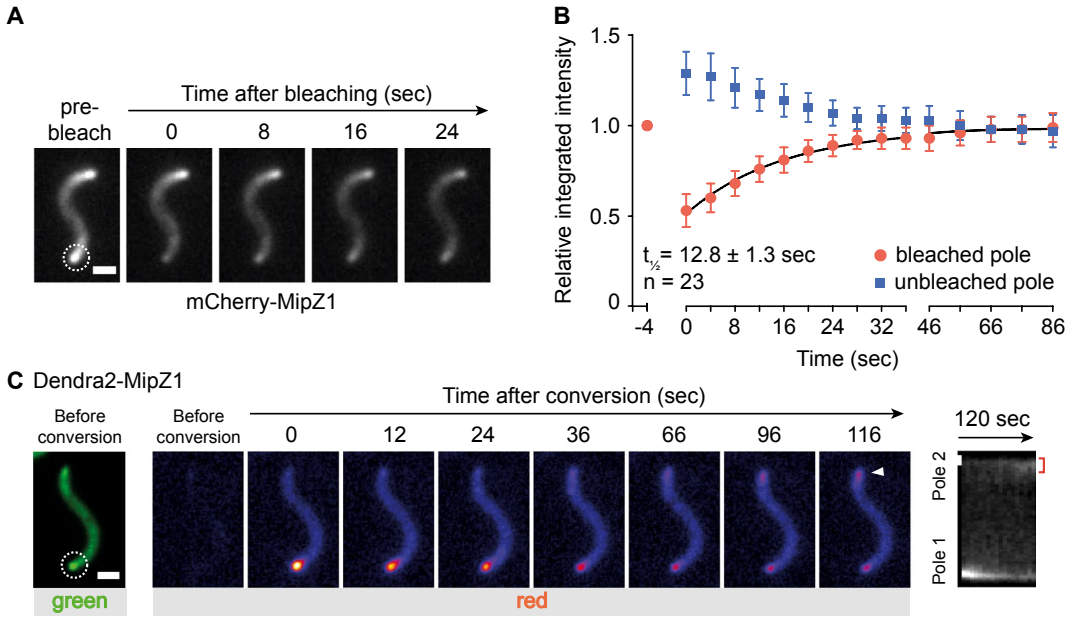

Fig. 3. Photokinetic analysis of MipZ1 dynamics.
A. FRAP analysis of mCherry-MipZ1 (strain eMTN025). Shown are images of a representative cell taken before and at the indicated time points after photobleaching. White dashed circle: bleached area.
B. Quantification of the fluorescence signals in (A). The first image ($t = 0$ s) was taken immediately after the laser pulse. Error bars: SD. $t_{½}$: fluorescence recovery half-time. A similar recovery half-time (13.8 ± 1.2 s; $n = 18$ cells) was obtained with the alternative strain eMTN032.
C. Photoconversion of Dendra2-MipZ1 in the WT background (strain eMTN030). Green channel: before photoconversion (white dashed circle: laser-illuminated area). Red channel: photoconverted protein after a 405 nm laser pulse. White arrowhead: presence of Dendra2-MipZ1 signal at the opposite non-photoconverted pole. The kymograph on the right shows the signal intensity (red channel) of photoconverted molecules along the cellular long axis (y-axis) over time (x-axis). The Dendra2-MipZ1 signal at the non-illuminated pole are indicated by a red bracket. Scale bars: 1 μm (micrographs) and 500 nm (kymograph).

background. The behavior of the fusion protein was essentially unchanged under this condition ($t_{½}$ ~11 s), supporting the notion that MipZ1 and MipZ2 act independently of each other (Fig. S4B). To directly visualize and further confirm the rapid exchange of MipZ1 between the two cell poles, we tagged the protein with the green-to-red photoconvertible fluorescent protein Dendra2. Subsequently, one of the cell poles was illuminated with a laser to induce photoconversion, and the redistribution of the newly generated red fluorescent Dendra2-MipZ1 molecules was monitored over time. The photoconverted fusion protein was detected at the opposite pole within only a few seconds after application of the laser pulse. At ~ 1 min post-photoconversion, the signal intensities at the two poles had reached equilibrium (Fig. 3C). This result is in agreement with the kinetics of fluorescence recovery observed in the FRAP experiment and provides direct evidence of an exchange of MipZ1 molecules between the two cell poles.

The ATPase activity of $MipZ_{Cc}$ has previously been shown to be essential for MipZ gradient formation in *C. crescentus*. When the protein was locked in the ATP-bound (dimeric) state by mutation of a conserved aspartic acid residue involved in nucleotide hydrolysis, it no longer accumulated near the cell poles but became tightly associated with the nucleoid, preventing FtsZ assembly throughout the entire cell (Thanbichler and Shapiro, 2006; Kiekebusch *et al.*, 2012). Introduction of an equivalent amino acid exchange (D43A) into MipZ1 from *M. gryphiswaldense* also abolished gradient formation, even when analyzed in the presence of native MipZ1, and led to a significant increase in cell length (Fig. 4A, E and F). To determine whether the delocalized mutant protein was freely diffusible or attached to the nucleoid, we assessed its mobility by FRAP analysis. The mCherry-$MipZ1^{D43A}$ fusion displayed a recovery half-time of ~ 43 s (Fig. 4B), indicating a significant ($p < 0.001$) decrease in its mobility compared to the wild-type protein (see Fig. 3B), consistent with nucleoid binding.

To further investigate the ATPase cycle of MipZ1, we aimed to determine the functional properties of MipZ1 in its monomeric state. Previous work has shown that the substitution of a highly conserved glycine residue in the dimer interface with valine prevented $MipZ_{Cc}$ dimerization, producing an exclusively monomeric variant of the protein (Thanbichler and Shapiro, 2006; Kiekebusch *et al.*, 2012). Cells producing a variant of *M. gryphiswaldense* MipZ1 carrying an equivalent mutation (mCherry-$MipZ1^{G15V}$) lacked the typical bipolar gradient. Instead, they displayed an elevated level of background fluorescence and distinct polar foci, likely reflecting the positions of ParB

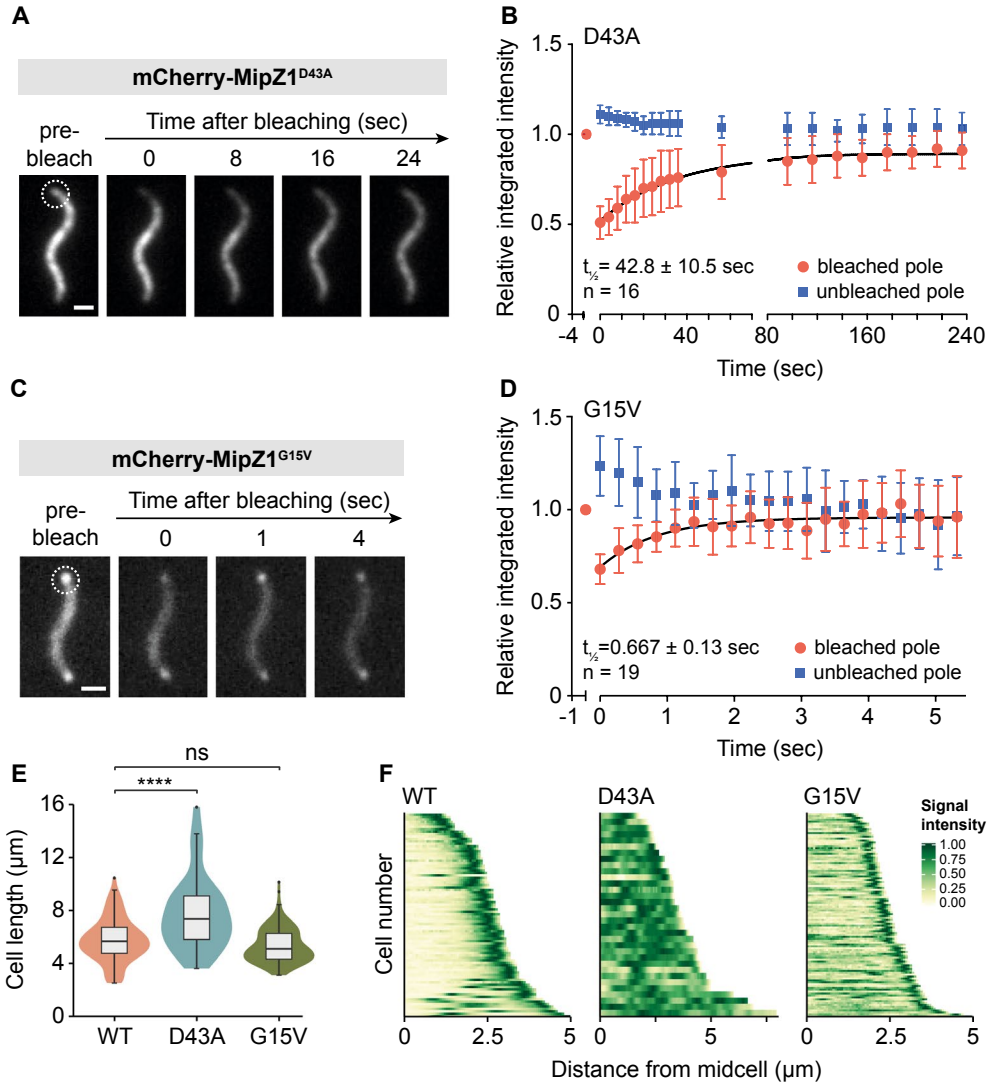

Fig. 4. Photobleaching analysis of MipZ1^{D43A} and MipZ1^{G15V}.
A. FRAP analysis of mCherry-MipZ1^{D43A} (strain eMTN028). Shown are images of a representative cell taken before and at the indicated time points after photobleaching. White dashed circle: bleached area. Scale bar: 1 µm.
B. Quantification of the fluorescence signals in (A). The first image (t = 0 s) was taken immediately after the laser pulse. Error bars: SD. $t_{½}$: fluorescence recovery half-time.
C. FRAP analysis of mCherry-MipZ1^{G15V}, performed as described for (A). Scale bar: 1 µm.
D. Quantification of the fluorescence signals in (C). The first image (t = 0 s) was taken immediately after the laser pulse. Error bars: SD. $t_{½}$: fluorescence recovery half-time.
E. Cell length distribution of strains producing wild type (WT) mCherry-MipZ1 (eMTN032) or the indicated mutant derivatives (eMTN028 and eMTN029). The data are represented as box plots and rotated kernel density plots, as described in Fig. 1B. n = 84 cells (WT), 33 cells (D43A) and 108 cells (G15V).
F. Subcellular localization of mCherry-MipZ1 (WT) and the indicated mutant derivatives. The graph shows a demographic analysis of the cells measured in (E), generated as described in the legend to Fig. 2F (****$p < 0.0005$; ns: not significant). Only the portion corresponding from midcell to the cell pole is shown for every cell.

(see below) (Fig. 4C, E and F). These polar assemblies were highly dynamic and exchanged molecules with a half-time of only 0.7 s, as determined by FRAP analysis (Fig. 4D).

Together, these data demonstrate that ATP binding and hydrolysis are required for proper gradient formation. Moreover, they suggest that the inhibitory effect on cell division may be exerted by the dimeric form of MipZ1 *in vivo*.

MipZ1 interacts with ParB

In *C. crescentus*, ParB plays a central role in MipZ$_{Cc}$ gradient formation, likely by stimulating the dimerization of

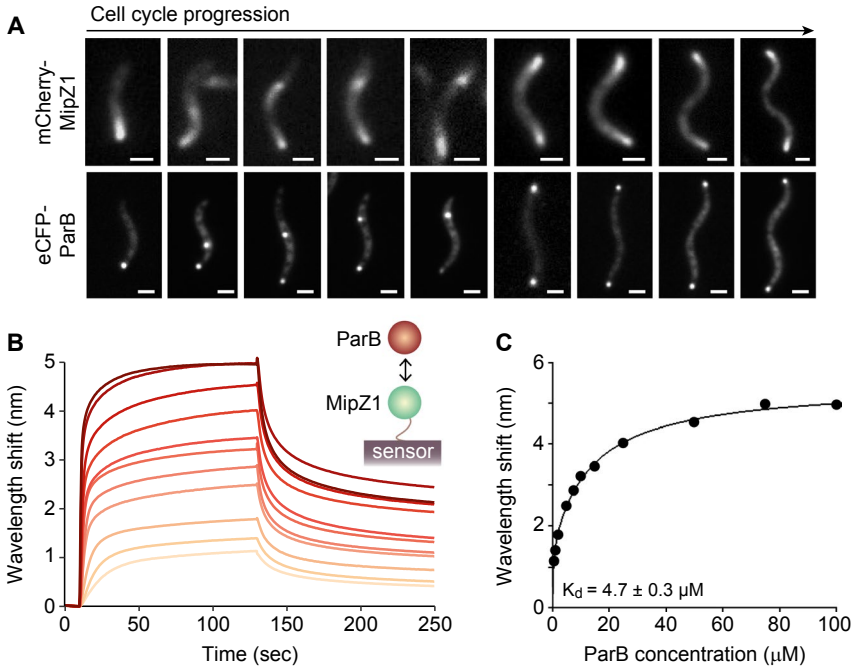

Fig. 5. Interaction of MipZ1 with ParB.
A. Fluorescence micrographs of *M. gryphiswaldense* cells producing mCherry-MipZ1 (strain eMTN025) or eCFP-ParB (strain eMTN031). Cells are arranged from left to right according to their putative cell cycle state. Note that the fusion proteins are produced in different strains. Scale bars: 1 μm.
B. Bio-layer interferometric analysis of the interaction between MipZ1 and ParB. Biotinylated MipZ1 was immobilized on a streptavidin-coated biosensor and probed with increasing concentrations of ParB (from 0.5 to 100 μM).
C. Binding analysis of the interaction between MipZ1 and ParB. The wavelength shifts measured at the end of the association phase (Bmax) were plotted against the protein concentration. The apparent equilibrium dissociation constant (K_d) of the MipZ1·ParB complex was obtained by fitting the data to a one-site saturation ligand binding model. The value indicates the average of two independent experiments (± SE).

MipZ$_{Cc}$ at the cell poles (Thanbichler and Shapiro, 2006; Kiekebusch *et al*., 2012). We therefore aimed to determine whether this protein also contributed to the localization of MipZ1 in *M. gryphiswaldense*. To this end, we followed the localization of mCherry-MipZ1 and eCFP-ParB over the course of the cell cycle. In shorter (younger) cells, MipZ1 was only detected at one of the cell poles (Fig. 5A). At later stages, cells displayed a second mCherry-MipZ1 focus, which appeared to move gradually to the opposite pole, finally yielding the typical bipolar gradient. Importantly, eCFP-ParB showed a similar transition from a unipolar to a bipolar pattern, suggesting a correlation between the movement of MipZ1 and ParB.

To determine whether MipZ1 binds to ParB directly, we purified the two proteins and conducted *in vitro* interaction analyses using bio-layer interferometry. For this purpose, biotinylated MipZ1 was immobilized on a streptavidin-coated sensor and probed with increasing concentrations of ParB (Fig. 5B). Analysis of the resulting binding curves revealed that the two proteins are able to interact efficiently in the absence of any cofactors, as reflected by an apparent equilibrium dissociation constant (K_d) of 4.7 μM (Fig. 5C). Notably, a similar behavior has previously been observed for the MipZ and ParB homologs of *C. crescentus* (K_d ~ 2 μM), suggesting the conservation of this interaction across species (Thanbichler and Shapiro, 2006).

MipZ1 binds to DNA in a non-specific and ATP-dependent manner

Our results indicated that dimerization drastically reduces the diffusion rate of MipZ1. To determine whether this effect was indeed mediated through association with the nucleoid, we analyzed the interaction of MipZ1 with DNA in an electromobility shift assay. In the presence of ATPγS (a slowly hydrolyzable analog of ATP), MipZ1 and its constitutively dimeric D43A variant drastically reduced the mobility of a linearized plasmid during electrophoresis, whereas no retardation was observed for monomeric MipZ1^{G15V} or nucleotide-free wild-type protein (Fig. 6A). These results indicate that MipZ1 indeed gains the ability to interact with non-specific DNA upon dimerization. To corroborate this finding, we performed localization studies in *Escherichia coli*, a species lacking MipZ homologs and a P*ar*AB*S* chromosome partitioning system. A wild-type mCherry-MipZ1 fusion was found to be largely dispersed throughout the cell (Fig. 6B), reminiscent of the results obtained for MipZ$_{Cc}$ (Kiekebusch *et al*., 2012). The

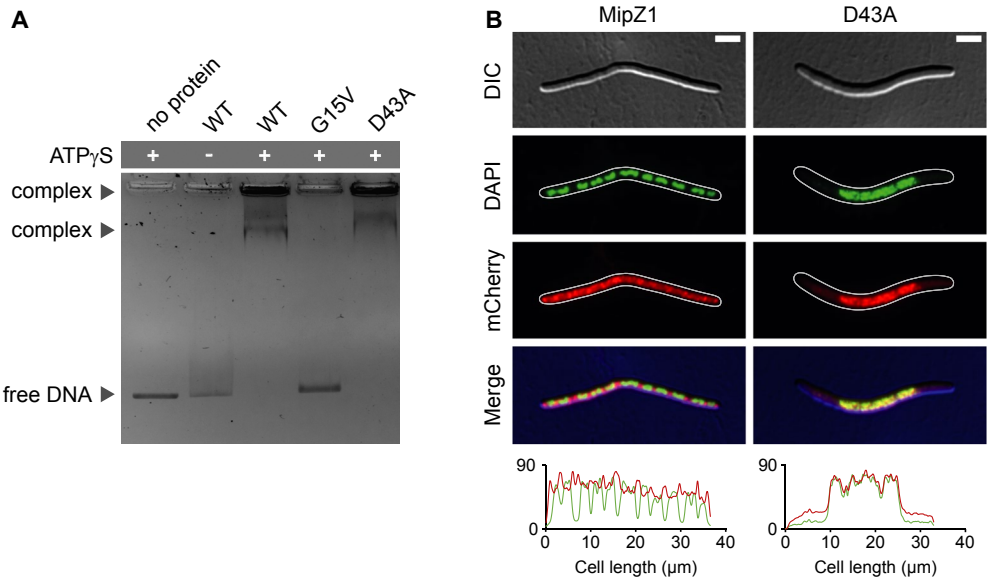

Fig. 6. Interaction of MipZ1 with DNA.
A. Gel mobility shift assay showing the DNA-binding activity of MipZ1. A non-specific DNA fragment was incubated with wild-type MipZ1 or its mutant derivatives in the presence or absence of ATPγS and subjected to gel electrophoresis.
B. *In vivo* interaction of MipZ1 with chromosomal DNA. *E. coli* cells producing mCherry-MipZ1 (strain eMTN036) or mCherry-MipZ1^{D43A} (strain eMTN038) were treated with cephalexin and chloramphenicol to inhibit cell division and condense the nucleoids, respectively, facilitating the interpretation of the data. Nucleic acids were stained with DAPI. Scale bars: 5 μm. The graph at the bottom shows a comparison of the mCherry (red) and DAPI (green) fluorescence intensity profiles.

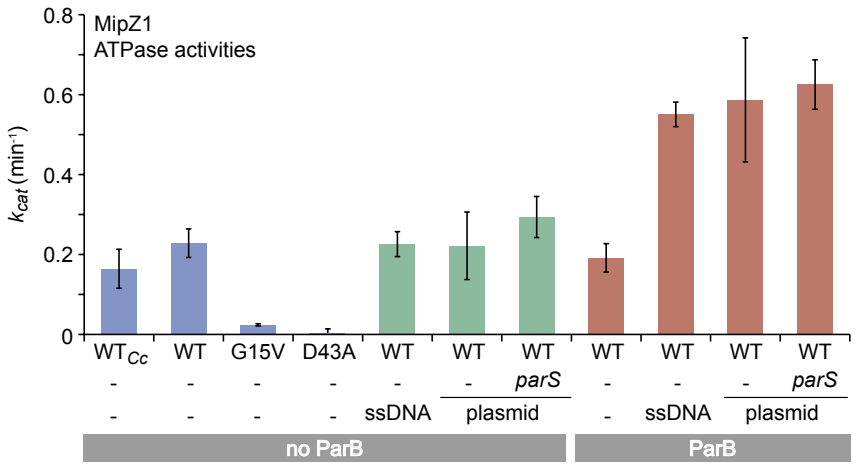

Fig. 7. ATPase activities of wild-type MipZ1 and its mutant derivatives. The indicated proteins were incubated in the absence or presence of ParB and/or DNA containing or not containing the *parS* sites from *C. crescentus*. MipZ$_{Cc}$ was analyzed as a reference. The turnover numbers (k_{cat}) shown represent the average of 2–8 independent experiments (± SE).

MipZ1^{D43A} variant, by contrast, strictly colocalized with the DAPI-stained nucleoid (Fig. 6B). Notably, similar results were obtained when we used this system to analyze the localization behavior of MipZ2 and its putatively dimeric MipZ2^{D43A} variant (Fig. S5). Thus, both MipZ homologs of *M. gryphiswaldense* appear to associate with the nucleoid in their dimeric form, a property that likely provides the basis for gradient formation (Figs 1F and 2D).

To investigate the effect of ParB and DNA on the ATPase cycle of MipZ1, we performed *in vitro* nucleotide hydrolysis assays using purified proteins. Wild-type MipZ1 was able to hydrolyze ATP with a turnover number (k_{cat}) of 0.23 min^{-1} (Fig. 7), a value similar to that measured for MipZ$_{Cc}$ (Fig. 7; Thanbichler and Shapiro, 2006). In contrast, its mutant derivative MipZ1^{D43A} essentially lacked catalytic activity (k_{cat} = 0.0014 min^{-1}), supporting the notion that it is locked in an ATP-bound state. The activity of the putatively monomeric variant, MipZ1^{G15V}, was severely impaired as well (k_{cat} = 0.024 min^{-1}), consistent with the idea that dimerization of MipZ1 is a prerequisite

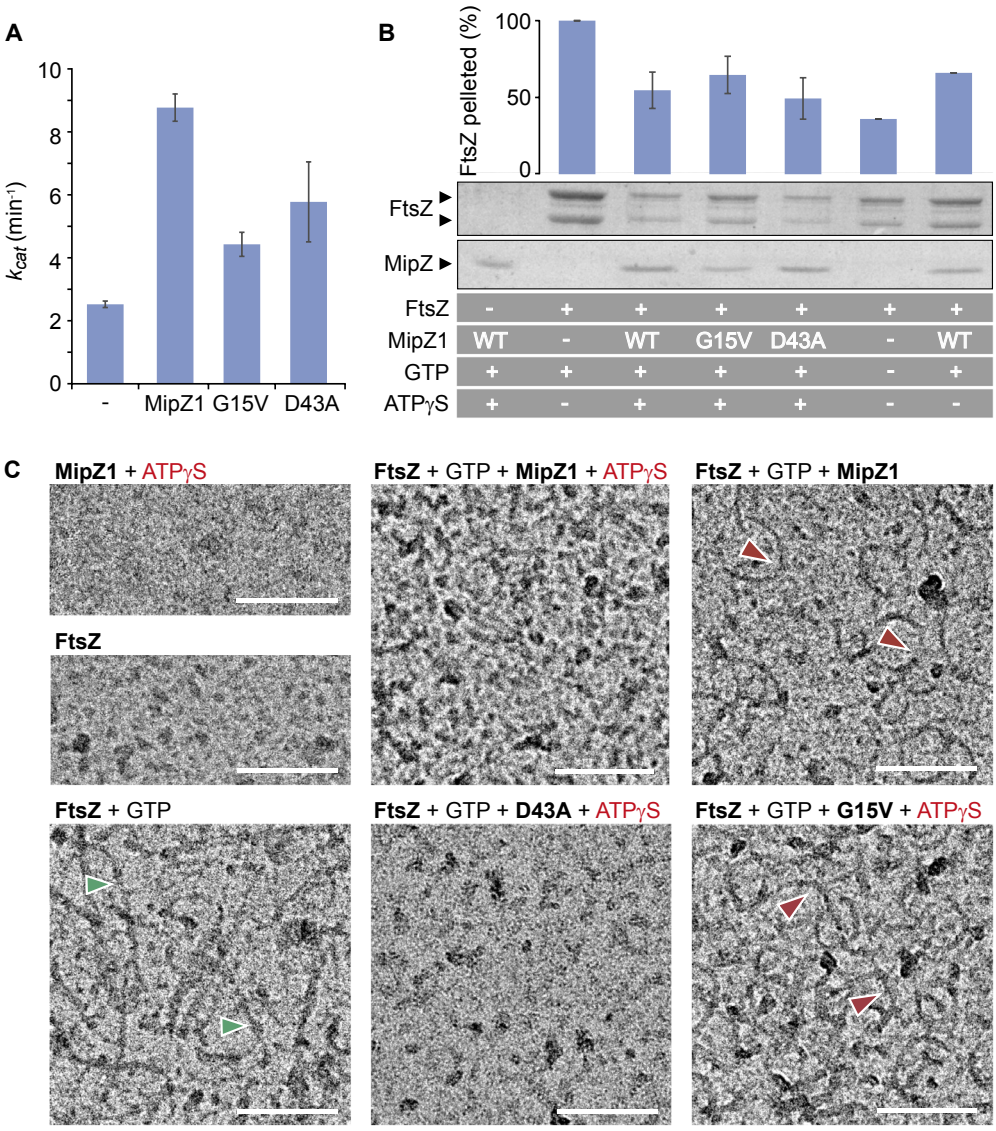

Fig. 8. Interaction of MipZ1 with FtsZ.
A. Effect of MipZ1 on the GTPase activity of FtsZ. FtsZ was incubated in the presence or absence of wild-type MipZ1 or its mutant derivatives. The turnover numbers (k_{cat}) shown represent the average of three independent experiments (± SE).
B. Effect of MipZ1 on the sedimentation of FtsZ. FtsZ was incubated in the presence or absence of MipZ1, ATPγS and/or GTP and subjected to ultracentrifugation. Shown is a representative SDS-gel loaded with the pellet fractions. The values plotted in the graph represent the average of 2–3 independent experiments.
C. Effect of MipZ on the structure of FtsZ polymers. FtsZ was incubated in the presence or absence of MipZ1, ATPγS and/or GTP, stained with uranyl acetate and visualized by transmission electron microscopy. Green arrowheads denote straight filaments, whereas red arrowheads indicate curved FtsZ filaments. Scale bars: 100 nm.

for nucleotide hydrolysis. Notably, the ATPase activity of MipZ1 was barely affected by the presence of a plasmid or single-stranded DNA (Fig. 7). Similarly, ParB alone did not have a stimulatory effect on the catalytic activity of MipZ1. However, when both plasmid or single-stranded DNA and ParB were included in the reaction, nucleotide hydrolysis was slightly accelerated (Fig. 7). The presence of *parS* sites did not have any additional stimulatory effect, despite the fact that ParB binds tightly to *parS*-containing DNA under the conditions used (Fig. S6). Collectively, these results resemble those obtained in *C. crescentus* (Thanbichler and Shapiro, 2006; Kiekebusch *et al.*, 2012), suggesting the conservation of the MipZ ATPase cycle.

MipZ1 inhibits FtsZ polymerization in vitro

The results obtained so far suggested that Z-ring assembly in *M. gryphiswaldense* is regulated by a gradient of

nucleoid-associated MipZ1 dimers. To further investigate the regulatory role of MipZ1 in FtsZ polymerization, we first examined its effect on the GTPase activity of FtsZ *in vitro* (Fig. 8A). When analyzed in the absence of other proteins, purified FtsZ from *M. gryphiswaldense* hydrolyzed GTP with a turnover number of 2.5 min^{-1}. Notably, addition of MipZ1 in complex with ATPγS led to an ~ 3.5-fold increase in its hydrolytic activity (k_{cat} = 8.8 min^{-1}). A similar result was obtained upon incubation of FtsZ with the constitutively dimeric $MipZ1^{D43A}$ variant (k_{cat} = 5.8 min^{-1}), suggesting that the MipZ1 dimer interacts with FtsZ, thereby affecting its GTPase cycle. Interestingly, unlike in the *C. crescentus* system (Thanbichler and Shapiro, 2006), the putatively monomeric $MipZ1^{G15V}$ variant also induced a moderate (~1.7-fold) increase in the FtsZ GTPase activity.

To determine whether the polymerization behavior of FtsZ was affected by its interaction with MipZ1, we performed sedimentation assays (Fig. 8B). In the presence of ATPγS, both MipZ or $MipZ1^{D43A}$ indeed caused a considerable decrease in the amount of FtsZ that was recovered from the pellet after centrifugation, indicating a reduction in the amount and/or length of FtsZ polymers. In line with the results of the GTPase assay, monomeric forms of MipZ1 (either $MipZ1^{G15V}$ or nucleotide-free MipZ1) were also able to inhibit FtsZ assembly, albeit to a lesser extent. Collectively, these results demonstrate that MipZ1 interacts with FtsZ, thereby altering its polymerization properties.

In order to visualize the changes in FtsZ assembly caused by MipZ1, we subjected protein samples to transmission electron microscopy. When incubated alone, *M. gryphiswaldense* FtsZ showed robust GTP-dependent polymerization, forming dense aggregates of straight or slightly bent filaments (Fig. 8C). These results are in agreement with previous work reporting the GTP-dependent assembly of this protein by dynamic light scattering (Müller *et al.*, 2014). Importantly, polymeric structures were no longer detectable after addition of MipZ1 or $MipZ1^{D43A}$ in complex with ATPγS (Fig. 8C), confirming the inhibitory effect of MipZ1 dimers on FtsZ assembly. Again, nucleotide-free MipZ1 or the constitutively monomeric $MipZ1^{G15V}$ variant also had a noticeable effect on FtsZ polymerization, giving rise to shorter filaments that were no longer straight but rather curved (Fig. 8C). This observation may explain the inhibitory effect on cell division induced by overproduction of $MipZ1^{G15V}$ *in vivo* (see Fig. 4E).

Discussion

The molecular mechanisms controlling bacterial division site placement have so far only been investigated in a few selected model species and appear to be highly diverse among different evolutionary lineages. In this study, we dissected the function of two MipZ homologs in the spiral-shaped alphaproteobacterium *M. gryphiswaldense* and show that the prototypical MipZ system of *C. crescentus* is partially conserved in this species. Although the two MipZ homologs of *M. gryphiswaldense* share high sequence similarity, their functions appear to differ significantly. Our results demonstrate that MipZ1 is critical for proper cell division (Fig. 1A and B) and represents a *bona fide* homolog of *C. crescentus* MipZ. The function of MipZ2, by contrast, still remains elusive, because in spite of its similarity to $MipZ_{Cc}$ and MipZ1, its absence did not cause any obvious phenotype (Fig. 2A–C). Interestingly, the localization patterns of MipZ1 and MipZ2 are diametrically different. Whereas MipZ1 consistently localized to the cell poles, likely driven by its interaction with the polar ParB·*parS* complexes (Pfeiffer *et al.*, 2019), its paralogue MipZ2 shows a unipolar localization in newborn cells and later relocates to the site of cell division, following FtsZ (Fig. 2F). This behavior is reminiscent of MipZ from *Rhodobacter sphaeroides*, which represents a functionally divergent class of MipZ proteins (Dubarry *et al.*, 2019) that are recruited to the cell division site and form a ring-like assembly at the inner face of the constricting Z-ring.

The need for a second MipZ system may be explained by the fact that cells of *M. gryphiswaldense* grow significantly longer (2–10 µm) than those of *C. crescentus* (1–2 µm). Considering the limited length of the bipolar MipZ1 gradient, MipZ1 alone may not be sufficient to ensure proper FtsZ assembly at midcell at later stages of the cell cycle. Interestingly, in *M. gryphiswaldense*, FtsZ remains mobile and poorly focused until MipZ2 accumulates at the division site (Fig. 2G). MipZ2 could therefore be an accessory factor that serves to stabilize the Z-ring. Alternatively, it may constitute a novel class of MipZ homologs that use the switch-like properties of MipZ to control the positioning or assembly of a protein other than FtsZ. A test of these hypotheses will require in-depth biochemical studies of MipZ2, which are, however, complicated by the fact that the protein is insoluble in purified form (data not shown). Apart from the biological role of MipZ2, it will be interesting to determine the factors mediating its localization to midcell or the cell poles.

Consistent with its functional similarity, MipZ1 displays biochemical properties that are comparable to those of its homolog in *C. crescentus*. Like other ParA-like ATPases (Ringgaard *et al.*, 2011; Scholefield *et al.*, 2011; Kiekebusch *et al.*, 2012), MipZ1 can exist in a monomeric and a dimeric form with distinct localization patterns and diffusion rates. Continuous oscillation between these two states, driven by ATP binding and hydrolysis, is required to establish the typical bipolar concentration gradient (Figs 3 and 4). As observed for $MipZ_{Cc}$, MipZ1 dimers have non-specific DNA-binding activity and thus associate

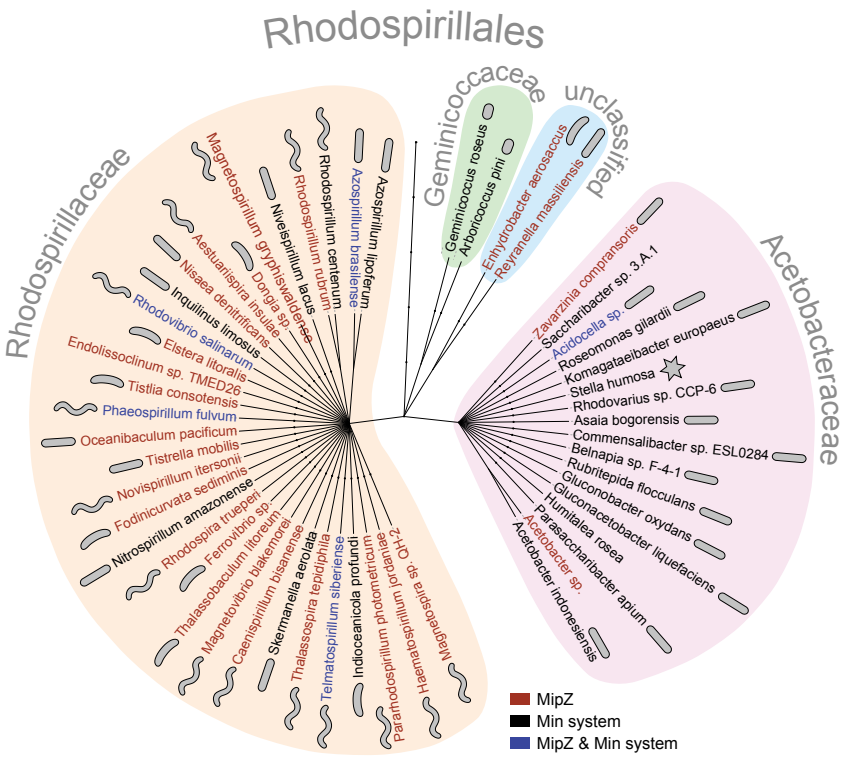

Fig. 9. Phylogenetic distribution of the MipZ and Min systems in the order *Rhodospirillales*. Genome sequences from the order *Rhodospirillales* were searched for homologs of *C. crescentus* MipZ (GenBank ACL95711.1) and *E. coli* MinC (GenBank AAC74260.1) using the BLASTp server (https://blast.ncbi.nlm.nih.gov). The phylogenetic relationship of positive species was then determined with phyloT (https://phylot.biobyte.de) and plotted with iTOL. Only one representative species is shown for each genus.

with the nucleoid, leading to a considerable decrease in their diffusion rate (Figs 4 and 6). Once they hydrolyze ATP, they dissociate into monomers, which are released from the DNA (Figs 4 and 6). Monomeric MipZ1 diffuses rapidly within the cell and interacts with ParB at the cell poles (Figs 4 and 5), thereby transitioning to the dimeric state again. After dissociation from the polar ParB·*parS* complex, MipZ1 dimers re-associate with pole-proximal regions of the nucleoid, where they remain tethered until ATP hydrolysis initiates the next localization cycle. A recent report showed that, in *M. gryphiswaldense*, inactivation of PopZ causes various cellular defects, including cell filamentation and acentric cell division (Pfeiffer *et al.*, 2019). These phenotypes may, at least in part, be explained by the failure of the mutant cells to recruit ParB to the cell poles and thus to establish a symmetric MipZ1 gradient, which further underscores the importance of MipZ1 for division site placement in this species.

Interestingly, unlike in the *C. crescentus* system, monomeric MipZ1 also had a noticeable effect on FtsZ, in particular on its GTPase activity (Fig. 8). However, the functional significance of this observation remains unclear, because *in vivo* most MipZ1 monomers interact with the polar ParB·*parS* complex and are therefore unable to affect the positioning of FtsZ at midcell. Nevertheless, it is conceivable that changes in the level of MipZ1 monomers, as potentially induced by duplication of the ParB·*parS* complex upon entry of the cells into S-phase, or the fast-diffusive cytoplasmic population of monomers could help to modulate the kinetics of Z-ring assembly.

M. gryphiswaldense has a second FtsZ gene, named FtsZm, which shares the core region of its canonical paralog but lacks the C-terminal linker and peptide (Müller *et al.*, 2014). It therefore retains the ability to polymerize but may have lost the capacity to bind to FtsZ tethers or stabilizers. FtsZm localizes at midcell, likely through interaction with FtsZ. However, it does not play a role in cell division but rather in magnetosome biomineralization (Müller *et al.*, 2014). It remains unclear whether MipZ1 or MipZ2 can interact with FtsZm. However, MipZ1 is likely to affect FtsZm polymerization at least indirectly through its regulatory effect on the canonical FtsZ homolog, thereby potentially coordinating cell division with the formation and cleavage of the magnetosome chain.

An analysis of the conservation of MipZ in the alphaproteobacterial order *Rhodospirillales* shows that MipZ homologs are largely limited to the family *Rhodospirillaceae*, which includes *M. gryphiswaldense* as well as a variety of other spiral-shaped or curved species (Fig. 9). The

rod-shaped or ovococcoid members of the other families, by contrast, mostly lack MipZ homologs and possess the Min system instead. This differential phylogenetic distribution may indicate that the gradient-forming MipZ homologs are better suited to control division site placement in cells with spirilloid morphologies, potentially because the oscillatory behavior of the Min system may be more difficult to maintain in these conditions. Notably, some members of the *Rhodospirillales* possess both a MipZ homolog and the MinCDE proteins. It will be interesting to investigate the selective advantage conferred by the combination of these independent regulatory systems.

Taken together, our findings show that *M. gryphiswaldense* uses two functionally distinct MipZ systems to ensure robust cell division. Gradient-forming MipZ systems may be widespread among the *Alphaproteobacteria*, especially in their spiral-shaped representatives, even though their cellular roles may have adapted to the specific needs of their host species.

Experimental procedures

Bacterial strains, plasmids and culture conditions

The bacterial strains, plasmids and oligonucleotides generated and used in this work are listed in Tables S1–S3. The construction of plasmids is detailed in the Supplemental Material. Strains of *M. gryphiswaldense* MSR-1 were grown under microoxic conditions in 2% oxygen-aerated modified flask standard medium (Heyen and Schüler, 2003) (FSM) containing 50 μM of ferric citrate at 30°C and moderate agitation (120 rpm). Media were supplemented with kanamycin (5 μg ml^{-1}) when appropriate. The expression of genes placed under the control of the P_{tet} promoter (Borg *et al*., 2014) was induced by addition of 50 ng ml^{-1} anhydrotetracycline. For localization studies, cells were analyzed in the early induction phase (3–5 h post induction), whereas longer induction times (> 12 h) were used for overexpression studies. FtsZ-mCherry localization was analyzed in the absence of inducer. *E. coli* strains DH5α, TOP10, Rosetta2(DE3)pLysS (Novagen) and WM3064 (W. Metcalf, unpublished) were grown in LB medium (Bertani, 1951) at 37°C. In the case of *E. coli* strain WM3064, which was used for the conjugative transfer of plasmids into *M. gryphiswaldense*, media were supplemented with 1 mM of DL-α,ε-diaminopimelic acid (DAP). *E. coli* strains carrying recombinant plasmids were grown in media containing additives at the following concentrations (μg ml^{-1}; liquid/solid medium) when required: kanamycin (25/50), ampicillin (50/200), chloramphenicol (20/30) or 2 % (w/v) glucose.

Epifluorescence microscopy

Images were acquired with (i) an Olympus BX81 microscope equipped with a 100/1.40 Oil UPLSAPO100XO objective and an Orca-ER camera (Hamamatsu), (ii) an Axio Observer.Z1 (Zeiss) microscope equipped with a Plan Apochromat 100/1.45 Oil DIC and a pco.edge sCMOS camera (PCO) or (iii) a DeltaVision Elite (GE Healthcare, Applied Precision) Olympus IX71 microscope equipped with a 100/1.40 Oil PSF objective (U-PLAN S-APO 100 Oil, 0.12 WD), a CoolSnap HQ2 CCD camera (Photometrics) and a four-color standard set Insight SSITM illumination module. *M. gryphiswaldense* cells were spotted onto a 1% of the 'MSR agarose pad' as described previously (Toro-Nahuelpan *et al*., 2016). Snap-shot images were taken at room temperature (25°C; for the Olympus BX81 microscope) or at 30°C (for the Delta Vision Elite microscope). Time-lapse series were recorded at 30°C using the DeltaVision Elite microscope. The fluorescence recovery after photobleaching (FRAP) and photoconversion assays are detailed in the Supplemental Material.

Transmission electron microscopy

To visualize cell morphology by conventional bright-field TEM analysis, cells were grown at 28°C under microaerobic conditions, fixed with formaldehyde (1%), concentrated 10-fold and adsorbed to carbon coated copper mesh grids (Plano, Germany). For the analysis of FtsZ polymerization, 5 μM FtsZ was incubated for 15 min at room temperature in buffer P (50 mM Hepes/NaOH, pH 7.2, 50 mM KCl, 5 mM $MgCl_2$) containing 2 mM of GTP and/or 1 mM of ATPγS in the presence or absence of 7.5 μM MipZ1 or its mutant derivatives. Glycerol concentrations were adjusted to the same values by compensating different volumes of protein solutions with storage buffer. Samples were incubated on glow-discharged carbon coated grids for 2 min, treated for 1 min with 2% of uranyl acetate and then washed twice with water. Micrographs were taken with a FEI CM200 (FEI, Netherlands) transmission electron microscope at an acceleration voltage of 160 kV. Images were captured with an Eagle 4k CCD camera using EMMenu 4.0 (TVIPS, Germany) and FEI software. Fiji software (Schindelin *et al*., 2012) was used for data analysis.

Plunge-freezing vitrification

Five microliter of *M. gryphiswaldense* culture was mixed with 2 μl of (two-fold concentrated) BSA-coated 15 nm colloidal gold clusters (Sigma-Aldrich, USA) to facilitate subsequent image alignment. The mixture was added onto glow-discharged Quantifoil R 2/1 holey carbon molybdenum grids (Quantifoil Micro Tools GmbH, Germany), manually blotted for 4 s, and embedded in vitreous ice by plunge-freezing in liquid ethane (< −170°C). The grids were stored in sealed boxes in liquid nitrogen until further use.

Cryo-electron tomography

Tomography was performed under low-dose conditions using a FEI Tecnai F30 G^2 Polara microscope equipped with a 300 kV field emission gun and a Gatan GIF 2002 post-column energy filter. A 3838 3710 Gatan K2 Summit Direct Detection Camera, operated in counting and dose-fractionation mode, was used for imaging. Data collection was performed at 300 kV, with the energy filter operated in the

zero-loss mode (slit width of 20 eV). Tilt series were acquired using Serial EM software (Mastronarde, 2005). The specimen was tilted about one axis with 1.5° increments over a typical total angular range of ± 60°. The cumulative electron dose applied during each tilt series was kept below 150 e^{-} $Å^{-2}$. To account for the increased specimen thickness at high tilt angles, the exposure time was multiplied by a factor of 1/cos α. The pixel sizes at the specimen level were 5.22 Å at an EFTEM magnification of 22,500 × *g*. Images were recorded at a nominal 5 to 8 μm defocus.

Tomogram reconstruction and segmentation

Tomograms were reconstructed with the IMOD package (Kremer *et al*., 1996). Tomographic reconstructions from tilt series were performed with the weighted back-projection approach using particles as fiducial markers. Aligned images were binned to the final pixel size of 31.32 Å. For tomographic reconstruction, the radial filter options were cut off: 0.5 and fall off: 0.05. The datasets using in this study comprised 10 tomograms for the Δ*mipZ1* strain and 9 tomograms for Δ*mipZ2* strain. Tomograms were treated with an anisotropic nonlinear diffusion denoising algorithm to improve the signal-to-noise ratio. Segmentation of the tomogram was achieved with Amira software on binned volumes with a voxel size of 31.32 Å. Membrane segmentation was performed using the Matlab-based segmentation tool termed TomoSegMemTV and the complementary package SynapSegTools (Martínez-Sánchez *et al*., 2014). Tomogram slices were obtained using 3dmod software from the IMOD package.

Protein overproduction and purification

To purify native MipZ1 protein or its mutant derivatives, Rosetta2(DE3)pLysS (Merck Millipore, Germany) was transformed with the appropriate plasmid and grown to an OD_{600} of 0.6. IPTG was added to a final concentration of 0.5 mM to induce protein synthesis. After 3 h of incubation, the culture was harvested by centrifugation and frozen at –80°C until further use. The cells were suspended in buffer B3 (2 ml per gram of cells) (50 mM NaH_2PO_4, 300 mM NaCl, 20 mM imidazole, adjusted to pH 8.0 with NaOH) containing 100 μg ml^{-1} of PMSF and 10 U ml^{-1} of DNase I, and lysed by three passages through a French press (16,000 psi). After centrifugation of the lysate for 60 min at 38,400 × *g*, the supernatant was passed through a membrane filter (0.45 μm pore size) and applied to a HisTrap HP 5 ml column (GE Healthcare) equilibrated with buffer B3. Protein was eluted with buffer B4 (50 mM NaH_2PO_4, 300 mM NaCl, 250 mM imidazole, adjusted to pH 8.0 with NaOH). Pooled fractions containing the protein of interest were dialysed against buffer B3 lacking imidazole in two steps (18 h and 4 h). The His-SUMO tag was cleaved by incubation of the protein with Ulp1-His protease in the presence of 1 mM DTT at 4°C for 2 h. Subsequently, untagged MipZ1 protein, Ulp1-His protease and His-SUMO were separated by chromatography on a HisTrap HP 5 ml column and elution with B4 buffer. The fractions containing pure MipZ1 protein were pooled, dialysed against PG buffer (50 mM Hepes/NaOH, pH 7.2, 50 mM KCl, 5 mM $MgCl_2$, 10% (v/v) glycerol) in two steps (18 h and 4 h), aliquoted, and stored at –80°C.

Native FtsZ and ParB were purified essentially as described for MipZ1 but using different buffers. In this case, cells were suspended in BZ3 buffer (50 mM Tris-HCl, 300 mM KCl, 20 mM imidazole, 10% (v/v) glycerol), the His-SUMO fusions were eluted from the column with BZ4 buffer (50 mM Tris-HCl, 300 mM KCl, 250 mM imidazole, 10% (v/v) glycerol) and dialyzed against CB buffer (50 mM Tris-HCl, 300 mM KCl, 10% (v/v) glycerol). After cleavage of the His-SUMO tag and further chromatographic purification, the native proteins were dialysed against PG buffer.

Protein concentrations were determined using the Roti-Nanoquant reagent (Carl Roth, Germany) with BSA as a standard.

Nucleotide hydrolysis assays

GTPase and ATPase activities were measured using a continuous, regenerative coupled-enzyme assay (Ingerman and Nunnari, 2005). All assays (total volume 150 μl) were performed at 25°C in PG buffer (50 mM Hepes/NaOH, pH 7.2, 50 mM KCl, 5 mM $MgCl_2$, 10% (v/v) glycerol) containing 20 U ml^{-1} of pyruvate kinase (Sigma-Aldrich), 20 U ml^{-1} of L-lactate dehydrogenase (Sigma-Aldrich), 600 μg ml^{-1} of NADH and 3 mM of phosphoenolpyruvate. GTPase reactions contained 3 μM of FtsZ, 2 mM of GTP, 1 mM of $ATP_{\gamma}S$ and 6 μM of MipZ (when appropriate). ATPase reactions contained 6 μM of MipZ, 1 mM of ATP and 0.2 μM of DNA and/or 12 μM of ParB (when appropriate). Glycerol concentrations were adjusted to the same values by compensating varying volumes of protein solution with storage buffer. The linear decrease in the absorbance of NADH at 334 nm was monitored for 40 min in an Epoch 2 microplate reader (BioTek Instruments, USA). Activity values were calculated using the extinction coefficient for NADH (6220 M^{-1} cm^{-1}) and an experimentally determined path length of 0.367 cm.

Bio-layer interferometry

Bio-layer interferometry was conducted using the BLItz system (Fortebio, USA) with Dip and Read Streptavidin Biosensors. For biotinylation, MipZ was incubated with a fourfold molar excess of wEZ-Link NHS-PEG4-Biotin (Thermo Fisher Scientific, USA) for 1 h at 4°C, followed by 15 min at room temperature. After the reaction, the protein was dialysed extensively against PG buffer. All assays were performed at room temperature in PG buffer containing 0.01% Triton X-100 and 0.01 mM BSA, with agitation at 2,200 rpm. Pre-equilibrated biosensors were incubated for 45 s with 4 μl of biotinylated MipZ1 and then washed for 30 s. The immobilized protein was then probed with various concentrations of ParB in a reaction volume of 4 μl. After an association phase of 90 s, the biosensor was transferred into protein-free reaction buffer to monitor the dissociation reaction. To determine the equilibrium dissociation constant (K_d), the maximal wavelength shifts measured at the end of the association phases were plotted against the corresponding protein concentrations. The data were then subjected to curve fitting using a one-site saturation ligand binding model in SigmaPlot (Systat Software, USA).

Electrophoretic mobility shift assays

Assays were performed in PG buffer in the presence or absence of $ATP_{\gamma}S$. Glycerol concentrations were adjusted to the same values by compensating varying volumes of protein solution with storage buffer. MipZ1 protein or its mutant derivatives (10 μM) were incubated with 10 nM of linearized plasmid pMCS-2 (Thanbichler *et al.*, 2007) as a source of double-stranded DNA for 15 min at room temperature. Subsequently, 5 μl of sample were applied for standard DNA agarose gel electrophoresis.

Sedimentation assays

FtsZ (3 μM) was incubated for 15 min at room temperature with 3 μM MipZ1 or its mutant derivatives, 2 mM GTP and/or 1 mM $ATP_{\gamma}S$ in buffer P. Glycerol concentrations were adjusted to the same values by compensating varying volumes of protein solution with storage buffer. The mixture was then centrifuged for 15 min at 385,900× *g* at 25°C using a Beckman MLA-130 rotor in a Beckman TL-100 ultracentrifuge. After immediate removal of the supernatants, the pellets were dissolved in 250 μl SDS sample buffer and incubated at 95°C for 5 min. Samples (5 μl) were loaded on a 10% SDS-polyacrylamide gel, and proteins were visualized with Coomassie brilliant blue after electrophoresis. For the quantification of protein bands, gels were imaged with a ChemiDoc MP imaging system (Bio-Rad, USA) and analyzed using Image Lab 5.0 (Bio-Rad).

Bioinformatic tools

Protein sequences were aligned with MAFFT v6 (Katoh *et al.*, 2002). Phylogenetic relationships were determined using the maximum likelihood method as implemented in RaxML (Stamatakis *et al.*, 2008) and visualized with the help of iTOL (Letunic and Bork, 2007; https://itol.embl.de) as described previously (Kiekebusch *et al.*, 2012). Structural models of proteins were generated with I-TASSER (Zhang, 2008) using $MipZ_{Cc}$ as a template and analyzed with the UCSF Chimera package (Pettersen *et al.*, 2004). Cell length measurements were performed with Fiji (Schindelin *et al.*, 2012) or BacStalk (Hartmann *et al.*, 2018). Boxplots were generated using R version 3.5.1 (http://www.r-project.org).

Acknowledgements

We thank Julia Rosum (Philipps-Universität Marburg) for excellent technical assistance. This work was supported by the German Research Foundation (DFG) (grant Schu 1080/9-2; to D.S.) and the European Research Council (ERC AdG Syntomagx, grant agreement no. 692637; to D.S.). Additional funding was provided by the DFG-funded Transregio Collaborative Research Center TRR 174 (project 269423233; to M.T. and M.B.) and a Max Planck Fellowship from the Max Planck Society (to M.T.). L.C.-G. was supported by the Horizon 2020 research and innovation programme of the European Union (MIPZ, grant agreement no. 659174). M.O.-V. was a fellow of the International Max Planck Research School for Environmental, Cellular and Molecular Microbiology (IMPRS-Mic).

Data availability statement

The data that support the findings of this study are included in the paper or available from the corresponding authors upon reasonable request.

Conflict of interest

The authors declare that there are no conflicts of interest.

Author contributions

M.T.-N. and D.S. conceived the study. M.T.-N., L.C.-G., M.T. and D.S. designed the study. M.T.-N. and F.-D.M. performed the *in vivo* experiments. M.T.-N. and L.C.-G. analyzed the data. M.T.-N., T.Z. and F.-D.M. generated strains. T.Z. performed the growth experiments and quantified the TEM data. L.C.-G. and M.O.-V. purified proteins and performed the biochemical analyses. J.M.P., M.B., M.T. and D.S. supervised the work. M.T.-N., L.C.-G., M.T. and D.S. wrote the manuscript, with input from all other authors.

References

Ben-Yehuda, S. and Losick, R. (2002) Asymmetric cell division in *B. subtilis* involves a spiral-like intermediate of the cytokinetic protein FtsZ. *Cell*, **109**, 257–266.

Bernhardt, T.G. and de Boer, P.A. (2005) SlmA, a nucleoid-associated, FtsZ binding protein required for blocking septal ring assembly over chromosomes in *E. coli*. *Molecular Cell*, **18**, 555–564.

Bertani, G. (1951) Studies on lysogenesis I: the mode of phage liberation by lysogenic *Escherichia coli*. *Journal of Bacteriology*, **62**, 293–300.

Bi, E.F. and Lutkenhaus, J. (1991) FtsZ ring structure associated with division in *Escherichia coli*. *Nature*, **354**, 161–164.

Bisson-Filho, A.W., Hsu, Y.P., Squyres, G.R., Kuru, E., Wu, F., Jukes, C., *et al.* (2017) Treadmilling by FtsZ filaments drives peptidoglycan synthesis and bacterial cell division. *Science*, **355**, 739–743.

Borg, S., Hofmann, J., Pollithy, A., Lang, C. and Schüler, D. (2014) New vectors for chromosomal integration enable high-level constitutive or inducible magnetosome expression of fusion proteins in *Magnetospirillum gryphiswaldense*. *Applied and Environment Microbiology*, **80**, 2609–2616.

Curtis, P.D. and Brun, Y.V. (2014) Identification of essential alphaproteobacterial genes reveals operational variability in conserved developmental and cell cycle systems. *Molecular Microbiology*, **93**, 713–735.

Ding, Y., Li, J., Liu, J., Yang, J., Jiang, W., Tian, J., *et al.* (2010) Deletion of the *ftsZ*-like gene results in the production of superparamagnetic magnetite magnetosomes

in *Magnetospirillum gryphiswaldense*. *Journal of Bacteriology*, **192**, 1097–1105.
Dubarry, N., Willis, C.R., Ball, G., Lesterlin, C. and Armitage, J.P. (2019) In vivo imaging of the segregation of the 2 chromosomes and the cell division proteins of *Rhodobacter sphaeroides* reveals an unexpected role for MipZ. *MBio*, **10**, e02515-18.
Erickson, H.P., Anderson, D.E. and Osawa, M. (2010) FtsZ in bacterial cytokinesis: cytoskeleton and force generator all in one. *Microbiology and Molecular Biology Reviews*, **74**, 504–528.
Flores, S.A., Howell, M., Daniel, J.J., Piccolo, R. and Brown, P.J.B. (2018) Absence of the Min system does not cause major cell division defects in *Agrobacterium tumefaciens*. *Frontiers in Microbiology*, **9**, 681.
Hartmann, R., van Teeseling, M.C.F., Thanbichler, M. and Drescher, K. (2018) BacStalk: a comprehensive and interactive image analysis software tool for bacterial cell biology. *bioRxiv*. https://doi.org/10.1101/360230.
Heyen, U. and Schüler, D. (2003) Growth and magnetosome formation by microaerophilic *Magnetospirillum* strains in an oxygen-controlled fermentor. *Applied Microbiology and Biotechnology*, **61**, 536–544.
Ingerman, E. and Nunnari, J. (2005) A continuous, regenerative coupled GTPase assay for dynamin-related proteins. *Methods in Enzymology*, **404**, 611–619.
Katoh, K., Misawa, K., Kuma, K. and Miyata, T. (2002) MAFFT: a novel method for rapid multiple sequence alignment based on fast Fourier transform. *Nucleic Acids Research*, **30**, 3059–3066.
Katzmann, E., Müller, F.D., Lang, C., Messerer, M., Winklhofer, M., Plitzko, J.M., *et al.* (2011) Magnetosome chains are recruited to cellular division sites and split by asymmetric septation. *Molecular Microbiology*, **82**, 1316–1329.
Kiekebusch, D., Michie, K.A., Essen, L.O., Löwe, J. and Thanbichler, M. (2012) Localized dimerization and nucleoid binding drive gradient formation by the bacterial cell division inhibitor MipZ. *Molecular Cell*, **46**, 245–259.
Komeili, A., Li, Z., Newman, D. and Jensen, G. (2006) Magnetosomes are cell membrane invaginations organized by the actin-like protein MamK. *Science*, **311**, 242–245.
Kremer, J.R., Mastronarde, D.N. and McIntosh, J.R. (1996) Computer visualization of three-dimensional image data using IMOD. *Journal of Structural Biology*, **116**, 71–76.
Letunic, I. and Bork, P. (2007) Interactive Tree Of Life (iTOL): an online tool for phylogenetic tree display and annotation. *Bioinformatics*, **23**, 127–128.
Li, Z., Trimble, M.J., Brun, Y.V. and Jensen, G.J. (2007) The structure of FtsZ filaments in vivo suggests a force-generating role in cell division. *EMBO Journal*, **26**, 4694–4708.
Lutkenhaus, J. (2007) Assembly dynamics of the bacterial MinCDE system and spatial regulation of the Z ring. *Annual Review of Biochemistry*, **76**, 539–562.
Marston, A.L., Thomaides, H.B., Edwards, D.H., Sharpe, M.E. and Errington, J. (1998) Polar localization of the MinD protein of *Bacillus subtilis* and its role in selection of the mid-cell division site. *Genes & Development*, **12**, 3419–3430.
Martínez-Sánchez, A., García, I., Asano, S., Lucic, V. and Fernández, J.J. (2014) Robust membrane detection based on tensor voting for electron tomography. *Journal of Structural Biology*, **186**, 49–61.
Mastronarde, D.N. (2005) Automated electron microscope tomography using robust prediction of specimen movements. *Journal of Structural Biology*, **152**, 36–51.
Müller, F.D., Raschdorf, O., Nudelman, H., Messerer, M., Katzmann, E., Plitzko, J.M., *et al.* (2014) The FtsZ-like protein FtsZm of *Magnetospirillum gryphiswaldense* likely interacts with its generic homolog and is required for biomineralization under nitrate deprivation. *Journal of Bacteriology*, **196**, 650–659.
Pettersen, E.F., Goddard, T.D., Huang, C.C., Couch, G.S., Greenblatt, D.M., Meng, E.C., *et al.* (2004) UCSF Chimera – a visualization system for exploratory research and analysis. *Journal of Computational Chemistry*, **25**, 1605–1612.
Pfeiffer, D., Toro-Nahuelpan, M., Bramkamp, M., Plitzko, J.M. and Schüler, D. (2019) The polar organizing protein PopZ is fundamental for proper cell division and segregation of cellular content in *Magnetospirillum gryphiswaldense*. *MBio*, **10**, e02716-18.
Radhakrishnan, S.K., Pritchard, S. and Viollier, P.H. (2010) Coupling prokaryotic cell fate and division control with a bifunctional and oscillating oxidoreductase homolog. *Developmental Cell*, **18**, 90–101.
Raskin, D.M. and de Boer, P.A. (1999) Rapid pole-to-pole oscillation of a protein required for directing division to the middle of *Escherichia coli*. *Proceedings of the National Academy of Sciences of the United States of America*, **96**, 4971–4976.
Ringgaard, S., Schirner, K., Davis, B.M. and Waldor, M.K. (2011) A family of ParA-like ATPases promotes cell pole maturation by facilitating polar localization of chemotaxis proteins. *Genes & Development*, **25**, 1544–1555.
Scheffel, A., Gruska, M., Faivre, D., Linaroudis, A., Plitzko, J.M. and Schüler, D. (2006) An acidic protein aligns magnetosomes along a filamentous structure in magnetotactic bacteria. *Nature*, **440**, 110–114.
Schindelin, J., Arganda-Carreras, I., Frise, E., Kaynig, V., Longair, M., Pietzsch, T., *et al.* (2012) Fiji: an open-source platform for biological-image analysis. *Nature Methods*, **9**, 676–682.
Scholefield, G., Whiting, R., Errington, J. and Murray, H. (2011) Spo0J regulates the oligomeric state of Soj to trigger its switch from an activator to an inhibitor of DNA replication initiation. *Molecular Microbiology*, **79**, 1089–1100.
Stamatakis, A., Hoover, P. and Rougemont, J. (2008) A rapid bootstrap algorithm for the RAxML Web servers. *Systematic Biology*, **57**, 758–771.
Thanbichler, M. and Shapiro, L. (2006) MipZ, a spatial regulator coordinating chromosome segregation with cell division in *Caulobacter*. *Cell*, **126**, 147–162.
Thanbichler, M., Iniesta, A.A. and Shapiro, L. (2007) A comprehensive set of plasmids for vanillate- and xylose-inducible gene expression in *Caulobacter crescentus*. *Nucleic Acids Research*, **35**, e137.
Toro-Nahuelpan, M., Müller, F.D., Klumpp, S., Plitzko, J.M., Bramkamp, M. and Schüler, D. (2016) Segregation of prokaryotic magnetosomes organelles is driven by treadmilling of a dynamic actin-like MamK filament. *BMC Biology*, **14**, 88.
Toro-Nahuelpan, M., Giacomelli, G., Raschdorf, O., Borg, S., Plitzko, J.M., Bramkamp, M., *et al.* (2019) MamY is a membrane-bound protein that aligns magnetosomes and

the motility axis of helical magnetotactic bacteria. *Nature Microbiology*, doi: 10.1038/s41564-019-0512-8.
Uebe, R. and Schüler, D. (2016) Magnetosome biogenesis in magnetotactic bacteria. *Nature Reviews Microbiology*, **14**, 621–637.
Wu, L.J. and Errington, J. (2004) Coordination of cell division and chromosome segregation by a nucleoid occlusion protein in *Bacillus subtilis*. *Cell*, **117**, 915–925.
Wu, L.J. and Errington, J. (2011) Nucleoid occlusion and bacterial cell division. *Nature Reviews Microbiology*, **10**, 8–12.
Yang, X., Lyu, Z., Miguel, A., McQuillen, R., Huang, K.C. and Xiao, J. (2017) GTPase activity-coupled treadmilling of the bacterial tubulin FtsZ organizes septal cell wall synthesis. *Science*, **355**, 744–747.
Yao, Q., Jewett, A.I., Chang, Y.W., Oikonomou, C.M., Beeby, M., Iancu, C.V., *et al.* (2017) Short FtsZ filaments can drive asymmetric cell envelope constriction at **355:** the onset of bacterial cytokinesis. *EMBO Journal*, **36**, 1577–1589.
Zhang, Y. (2008) I-TASSER server for protein 3D structure prediction. *BMC Bioinformatics*, **9**, 40.

Supporting Information

Additional supporting information may be found online in the Supporting Information section at the end of the article.